Comprehensive peak-width analysis in matter-wave diffraction under grazing incidence conditions

Lee Yeong Kim,[1] Do Won Kang,[2,*] Jong Chan Lee,[2] Eunmi Chae,[3] Wieland Schöllkopf,[4] and Bum Suk Zhao[1,2,†]
[1]*Department of Physics, Ulsan National Institute of Science and Technology, Ulsan 44919, Republic of Korea*
[2]*Department of Chemistry, Ulsan National Institute of Science and Technology, Ulsan 44919, Republic of Korea*
[3]*Department of Physics, Korea University, Seongbuk-gu, Seoul 02841, Republic of Korea*
[4]*Fritz-Haber-Institut der Max-Planck-Gesellschaft, Faradayweg 4-6, 14195 Berlin, Germany*

(Received 17 January 2024; accepted 5 June 2024; published 12 July 2024)

Thermal-energy atom scattering at a surface under grazing incidence conditions is an innovative method for investigating dispersive atom-surface interactions with potential application in quantum sensing interferometry. The complete establishment of this technique requires a detailed peak analysis, which is yet to be achieved. We examine peak-width fluctuations in atomic and molecular beams diffracted by a grating under grazing incidence conditions. Careful measurements and analyses of the diffraction patterns of He atoms and D_2 molecules from three square-wave gratings with different periods and radii of curvature enable the identification of factors influencing the peak-width variations as a function of incidence angle. The effects of macroscopic surface curvature, grating magnification, and beam emergence are substantial under these conditions but negligible for incidence angles close to the normal. Our results shed light on the phenomena occurring in grazing incidence thermal-energy atom scattering.

DOI: 10.1103/PhysRevA.110.013313

I. INTRODUCTION

X-ray, electron, neutron, and atom diffraction techniques are well-established methods for studying the crystal structures of materials and their changes over time. In diffraction experiments, the width of the diffraction peak, along with its intensity and position, is a critical parameter for sample analysis. For example, peak-width analysis has been employed to estimate crystallite or grain sizes and crystal strains in x-ray powder diffraction [1–4] and in grazing incidence x-ray scattering [5,6]. In thermal-energy atom scattering (TEAS), the broadening of peak widths provides insights into temperature-induced alterations in surface morphology [7] and the density of defects such as steps on a crystal surface [8,9].

The design of optical elements such as mirrors and gratings for x-ray and matter-wave optics also necessitates a comprehensive investigation of the widths of scattering peaks. X rays have been focused efficiently using cylindrical concave mirrors by minimizing peak-broadening effects [10–12]. Recently, this endeavor has also been extended to He atoms [13]. Furthermore, understanding wavelength-dependent peak-width broadening is essential for atom monochromators [14]. Thus, analyzing peak widths is crucial for developing new methodologies and technologies based on wave diffraction.

Grazing incidence thermal-energy atom scattering (GITEAS) at a surface offers a unique approach that can complement conventional TEAS, akin to the relationship between x-ray scattering and grazing incidence x-ray scattering. The lower effective energy and longer wavelength toward the surface for GITEAS make it more sensitive to weak interactions and less responsive to surface roughness. As a result, GITEAS has become valuable for studying the dispersive interaction of atoms with a surface [15–17]. Furthermore, microstructure-grating interferometry with GITEAS can be applied for quantum sensing in conjunction with monolithic atom interferometry using TEAS [18].

The versatile applications of GITEAS necessitate a precise peak-width analysis. However, under grazing incidence conditions, the peak widths are strongly influenced by an infinitesimal curvature (curvature radius of a few kilometers) and the diffraction direction near a surface, which results in unusual variations in peak widths. The presence of abnormally wide or narrow peaks further complicates the analysis. Furthermore, the traditional peak-width analysis scheme used in TEAS is insufficient for GITEAS, which highlights the need for a more sophisticated approach.

In this article we report a comprehensive analysis of peak widths for GITEAS. By adjusting the grating and incident-beam properties, we investigate various factors contributing to peak-width variations, such as the macroscopic surface curvature, grating magnification, incident-beam divergence, and angular dispersion. He atoms (D_2 molecules), with mean de Broglie wavelengths λ of 330 or 140 pm (140 pm), are diffracted at grazing incidence angles up to 30 mrad by three gratings of different periods and macroscopic curvatures. By comparing the measured peak widths with calculated widths, we identify the dominant factors influencing the variations in peak width. This resolves any potential ambiguities in the data analysis caused by extraordinary peak widths.

*Contact author: dowon5961@unist.ac.kr
†Contact author: zhao@unist.ac.kr

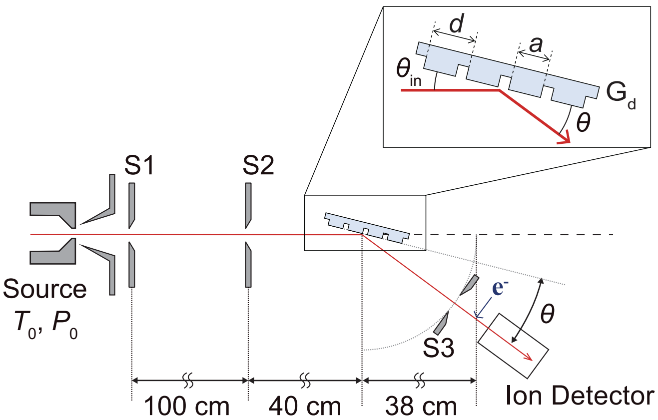

FIG. 1. Schematic of the experimental setup. The distances between the components are not drawn to scale. The incidence and detection angles θ_{in} and θ, respectively, are measured with respect to the grating surface. The inset illustrates a grating with d and a representing its period and strip width, respectively.

II. EXPERIMENTAL SETUP

A. Atomic- and molecular-beam apparatus

Our atom optics apparatus is characterized by a tightly collimated incident beam and high-angular-resolution detector and enables precise peak-width measurements. Further details of the setup can be found in Refs. [16,19]. Here we focus on the aspects of the apparatus pertinent to the data analysis presented in this study. A continuous beam of He or D_2 is formed by supersonic expansion of the corresponding pure gas from a source cell.

The beam is collimated using two slits (S1 and S2) positioned 100 cm apart as shown in Fig. 1. The widths of these slits, W_{S1} and W_{S2}, are 20 μm, except for one set of data, referred to as tight collimation, where $W_{S1} = 10$ μm and $W_{S2} = 15$ μm. The incident and scattered beams are detected by precisely rotating a mass spectrometer with electron-bombardment ionization. The rotational axis of the detector is located 40 cm downstream from S2. A third slit (S3) with a width of $W_{S3} = 25$ μm is positioned just before the detector. The distance between the rotational axis and S3, referred to as the grating-detector distance, is $L = 38$ cm.

B. Velocity distributions of atomic and molecular beams

The source temperature T_0 and pressure P_0 influence the particle velocity distributions. We use three sets of source conditions, viz., gas species, T_0, and P_0: (He, 9.0 K, 0.5 bar), (He, 52 K, 26 bars), and (D_2, 52 K, 2 bars). For each set of conditions, we observe a velocity distribution, from which the mean velocity v, full width at half maximum (FWHM) Δv, and corresponding mean de Broglie wavelength λ are determined (see Fig. 2). Accordingly, we obtain three corresponding sets of incident-beam properties, including v, Δv, and λ, i.e., (304 m/s, 2.3 m/s, 330 pm), (733 m/s, 5.9 m/s, 140 pm), and (736 m/s, 79 m/s, 140 pm), respectively, which are used to explore the effects of λ and Δv separately. The ratios $v/\Delta v$ for the He atom beams are 133 and 124 at the two different T_0 values, which are similar. In contrast, for the D_2 molecular beam $v/\Delta v = 9.3$.

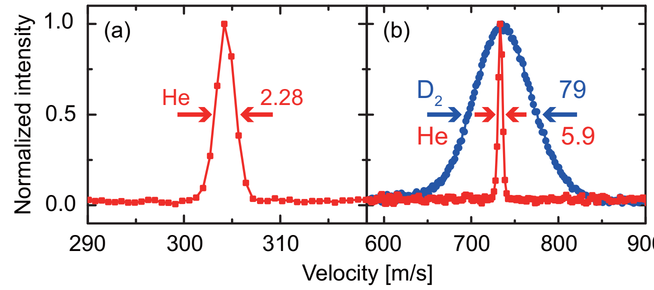

FIG. 2. Measured velocity distributions of He (red squares) and D_2 (blue circles) at (a) $T_0 = 9$ K and (b) $T_0 = 52$ K. The intensity is scaled to the peak values. The mean velocities are found to be (a) 304 m/s and (b) 730 m/s. For $P_0 = 0.5$ and 26 bars at $T_0 = 9$ and 52 K, respectively, the FWHM values for the He atom beams are 2.28 and 5.9 m/s. In contrast, the velocity width of the D_2 molecular beam is 79 m/s at $T_0 = 52$ K.

C. Fabrication and characterization of the diffraction gratings

We employ three square-wave gratings with varying periods d and strip widths a: G_1 with $d = 1$ μm and $a = 0.25$ μm, G_{20} with $d = 20$ μm and $a = 10$ μm, and G_{400} with $d = 400$ μm and $a = 200$ μm. Although nominally a plane, the grating surfaces exhibit small circular curvatures. Under grazing incidence conditions the curvature in the direction perpendicular to the incident plane affects the peak width only negligibly [20,21]. Therefore, we consider the gratings as cylindrical with their curvature radii R. For concave and convex gratings, $R > 0$ and $R < 0$, respectively. The estimated R values of G_1, G_{20}, and G_{400} are 30, −210, and 1800 m, respectively.

Gratings G_1 and G_{20} are microstructured arrays, each measuring 56 mm in length, consisting of 110-nm-thick chromium strips that are 5 mm in length and are deposited on a 2-mm-thick quartz surface. In contrast, G_{400} is an array featuring parallel photoresist strips with a thickness of 1 μm, a width of 200 μm, and a length of 4 mm. These strips are located on a commercial gold mirror (Thorlabs PFSQ20-03-M03), which is 6 mm thick and has a surface area of 50.8×50.8 mm^2. Only the strips were exposed to the incident atomic beam for all the angles of incidence examined in this study. Table I provides a summary of the properties of these gratings that are pertinent to variations in peak width, including their period d and radius of curvature R.

III. RESULTS

Figure 3 shows angular spectra for the three gratings measured at different experimental conditions for various incidence angles. The graphs represent the He^+ or D_2^+ signal as a

TABLE I. Grating properties relevant to the peak-width variation.

Grating	Period d (μm)	Curvature radius R (m)
G_1	1	30
G_{20}	20	−210
G_{400}	400	1800

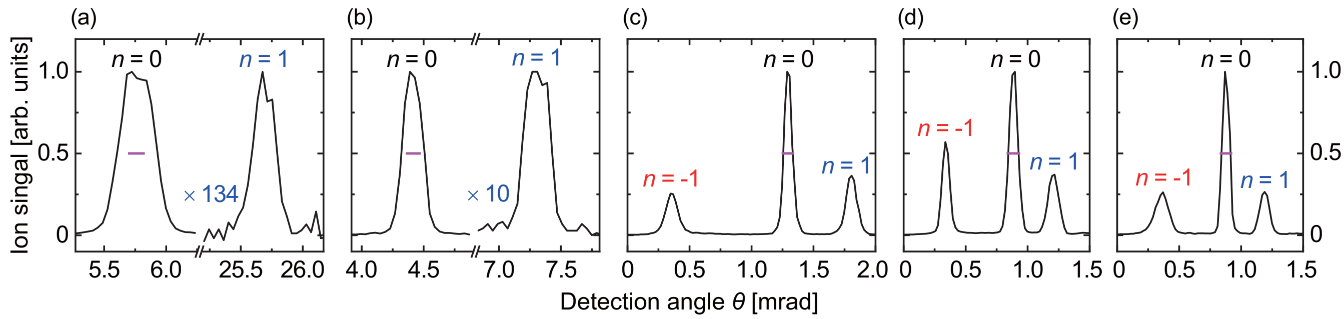

FIG. 3. Measured angular spectra of matter-wave beams of (a)–(d) He and (e) D_2 diffracted by gratings (a) G_1, (b) G_{20}, and (c)–(e) G_{400} at incidence angles θ_{in} of (a) 5.77, (b) 4.41, (c) 1.29, (d) 0.89, and (e) 0.88 mrad and mean de Broglie wavelengths λ of (a)–(c) 330 pm and (d) and (e) 140 pm. The horizontal bar near the specular peak indicates the corresponding width w_{in} of the beam with no grating installed. In (a) and (b) the first-order peak is magnified for clarity.

function of the detection angle θ. Here θ_{in} and θ are measured with respect to the grating surface. Numbers n indicate the diffraction order assigned to each peak. The peak positions θ_n and FWHM values w_n of the nth-order diffraction beams are determined by fitting each peak to a single Gaussian function. Similarly, we determine the FWHM w_{in} of the incident-beam spectrum when the grating is removed from the beam path.

A peak-width analysis reveals unexpected irregular hierarchies of w_n for the five cases of Fig 3: (a) $w_0 > w_1 > w_{\text{in}}$, (b) $w_1 > w_0 > w_{\text{in}}$, (c) $w_{-1} > w_{\text{in}} \approx w_1 > w_0$, (d) $w_{\text{in}} > w_1 > w_0 > w_{-1}$, and (e) $w_{-1} > w_{\text{in}} > w_1 > w_0$. Generally, in TEAS, diffraction peak widths increase with $|n|$ owing to the angular dispersion [22,23], and an increase of the specular width w_0 with respect to w_{in} can be attributed to surface defects [24]. Therefore, the unexpected hierarchies could lead to misinterpretation of the underlying physics and errors in peak assignment.

To study the peak-width variations systematically, we plot w_n as a function of θ_{in} for the five experimental conditions in Fig. 4. Each graph includes horizontal dotted lines indicating w_{in} and vertical dashed lines representing the Rayleigh incidence angle of negative-first-order diffraction-beam emergence ($\theta_{\text{R},-1}$). When $\theta_{\text{in}} = \theta_{\text{R},-1}$, the negative-first-order diffraction beam emerges from the grating and propagates parallel to its surface; in this case, $\theta_{-1} = 0$ [25,26].

The relationship between w_n and θ_{in} varies under different experimental conditions and for individual diffraction orders. Furthermore, the inconsistent hierarchies among w_0, w_1, and w_{-1} change with θ_{in}. Several factors contribute to these variations: (i) the macroscopic curvature of the grating surface, (ii) grating magnification, (iii) diffraction-beam spread resulting from the divergence of the incident beam, and (iv) angular dispersion due to the nonmonochromatic nature of the beam. Among these factors, (i) pertains to a property of the grating, (ii) results from the diffraction principle, and (iii) and (iv) are determined by the incident-beam properties.

The macroscopic curvature of the grating surface accounts for the variation in w_0 shown in Fig. 4. The magnitude of $|R|$ directly influences the steepness of the decrease in w_0. Additionally, when $R > 0$ ($R < 0$), w_0 increases (decreases) asymptotically toward w_{in} with θ_{in} as illustrated in Fig. 4(a) [Fig. 4(b)]. Furthermore, the steep increase in w_{-1} with decreasing θ_{in} in Figs. 4(a) and 4(e) is attributed to angular dispersion. Finally, the hierarchical order of $w_1 > w_0 > w_{-1}$ shown in the inset of Fig. 4(d) results from the grating magnification.

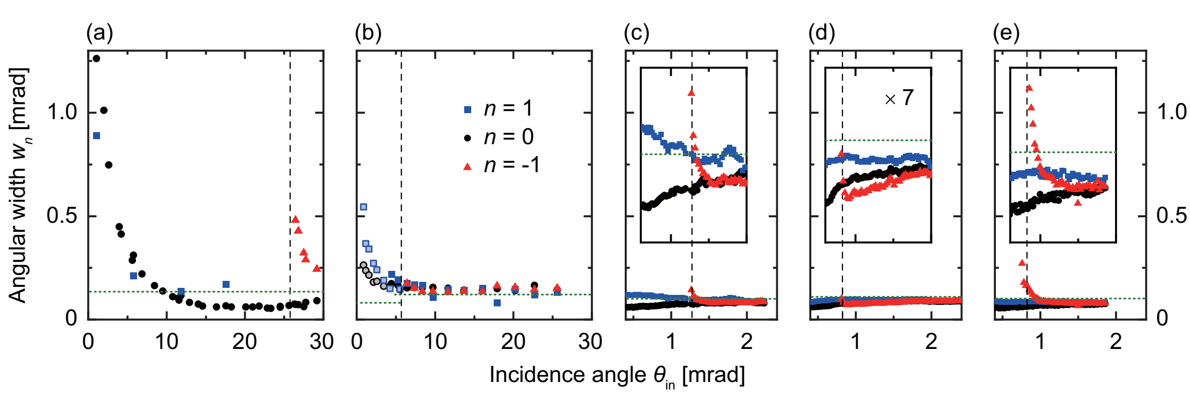

FIG. 4. Angular FWHM of the nth-order diffraction peak w_n as a function of the incidence angle θ_{in} for (a) G_1 of $R = 30$ m, (b) G_{20} of $R = -210$ m, and (c)–(e) G_{400} of $R = 1800$ m. The experimental conditions are the same as those in Fig. 3. The vertical dashed line denotes the Rayleigh incidence angle of the negative-first-order diffraction beam, referred to as $\theta_{\text{R},-1}$, where the negative-first-order diffraction beam emerges from the grating surface. The horizontal dotted line represents the width of the incident beam w_{in}. In (b), pale colored symbols within the range of θ_{in} from 0.5 to 5.5 mrad illustrate data obtained with tight collimation, resulting in a narrower w_{in} of 0.081 mrad (horizontal thick dotted line). The insets in (c)–(e) show sevenfold magnifications of the corresponding data series.

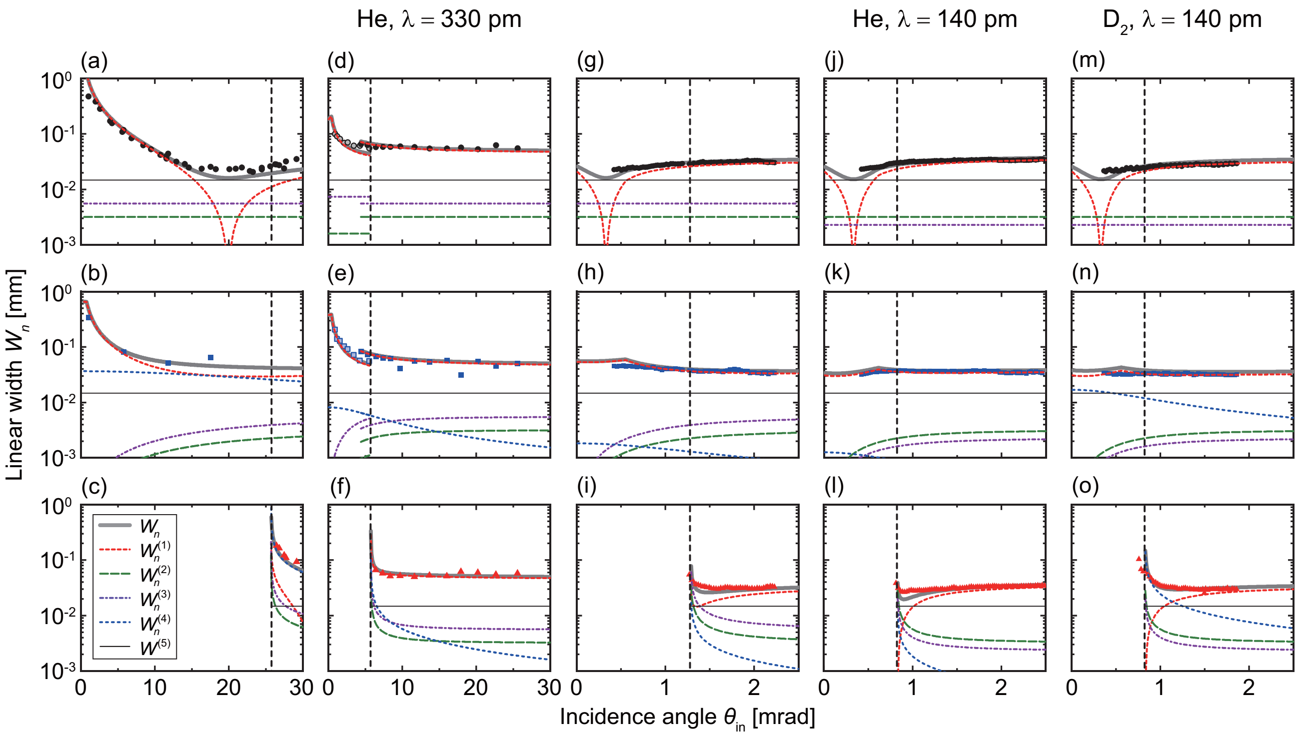

FIG. 5. Comparison between the measured (symbols) and calculated (solid curves) linear widths W_n of the nth-order diffraction beam for gratings (a)–(c) G_1, (d)–(f) G_{20}, and (g)–(o) G_{400}. The experimental conditions for (a)–(c), (d)–(f), (g)–(i), (j)–(l), and (m)–(o) are the same as those in Figs. 4(a)–4(e), respectively. The data are listed sequentially from the top for $n = 0$, 1, and -1. The W_0, W_1, and W_{-1} are plotted separately with the calculated $W_n^{(1)}$, $W_n^{(2)}$, $W_n^{(3)}$, $W_n^{(4)}$, and $W^{(5)}$.

IV. PEAK-WIDTH MODEL

Factors (i)–(iv) contribute to w_n differently depending on n, λ, and $\theta_{\rm in}$, which can be formulated by the approximate equation for a linear width $W_n = Lw_n$, i.e., $W_n = \sqrt{[W_n^{(1)}]^2 + [W_n^{(2)}]^2 + [W_n^{(3)}]^2 + [W_n^{(4)}]^2 + [W^{(5)}]^2}$, where

$$W_n^{(1)} = \left(\frac{1}{o} + \frac{1}{L} - \frac{1}{f_n}\right) L W_{\rm G} \frac{\sin\theta_n}{\sin\theta_{\rm in}}, \quad (1)$$

$$W_n^{(2)} = \frac{2.355}{4} \frac{W_{\rm S1}}{o} L \frac{\sin\theta_{\rm in}}{\sin\theta_n}, \quad (2)$$

$$W_n^{(3)} = 0.884 \frac{\lambda}{W_{\rm S2}} L \frac{\sin\theta_{\rm in}}{\sin\theta_n}, \quad (3)$$

$$W_n^{(4)} = \left(\frac{|n|\lambda}{d}\right) \frac{\Delta v}{v} \frac{1}{\sin\theta_n} L, \quad (4)$$

and

$$W^{(5)} = \frac{2.355}{4} W_{\rm S3}. \quad (5)$$

In these equations, $o = 1.4$ m represents the object distance, f_n denotes the focal length of the nth-order diffraction beam, and $W_{\rm G}$ denotes the width of the incident beam at the center of the grating. We determine $W_{\rm G}$ from the width of the incident beam at the third slit S3, $W_{\rm in}$. The latter is derived from the observed angular width as $W_{\rm in} = Lw_{\rm in}$. Because S1 constrains the effective source size of the matter-wave beam, we approximate the object as a Gaussian distribution with a standard deviation of $W_{\rm S1}/4$. Similarly, the boxcar-shaped function defined by S3 is approximated as a Gaussian function with a standard deviation of $W_{\rm S3}/4$.

The macroscopic curvature of the grating represented by R is relevant to its focal length. Under grazing incidence conditions, the object distance o and image distance i_n of the nth-order beam satisfy the thin lens equation $1/o + 1/i_n = 1/f_n$. The term in large parentheses of Eq. (1) then represents the focusing error ϵ_n and the product $\epsilon_n L W_{\rm G}$ is the width of the (de)focused incident beam at the detection plane [27]. Image distance, focal length, and focusing error vary with R and $\theta_{\rm in}$, as detailed in the Appendix. Specifically, f_0 can be expressed as $f_0 = R\sin\theta_{\rm in}/2$ [10,13]; therefore, i_n (or ϵ_n) can be determined based on the values of R and $\theta_{\rm in}$, as illustrated in Fig. 6.

The grating magnification given by $M_n = \sin\theta_n/\sin\theta_{\rm in}$, also known as anamorphic magnification, represents the ratio of the width of a collimated diffracted beam to that of a collimated incident beam [28]. When considering a collimated beam ($o \to \infty$) incident on a flat grating ($f_n \to \infty$), $W_n^{(1)}$ characterizes the grating magnification.

The width $W_n^{(2)}$ describes the effect of the geometrical incident-beam divergence of approximately $W_{\rm S1}/o$ on the diffraction-beam spread $\Delta\theta_n$. When $W_{\rm S1} = 20$ μm, $W_n^{(2)} = 3.2$ μm for the specular peak, which is negligible. In contrast, $W_n^{(2)}$ becomes significant when $\theta_{n<0} \to 0$, as happens when $\theta_{\rm in}$ approaches the Rayleigh angle of beam emergence $\theta_{{\rm R},n}$.

Slit diffraction at S2 contributes additional incident-beam divergence $\Delta\theta_{\rm in,SD}$, which is responsible for $W_n^{(3)}$. In the Fraunhofer limit, $\Delta\theta_{\rm in,SD} = 0.844\lambda/W_{\rm S2}$. Similar to $W_n^{(2)}$, this

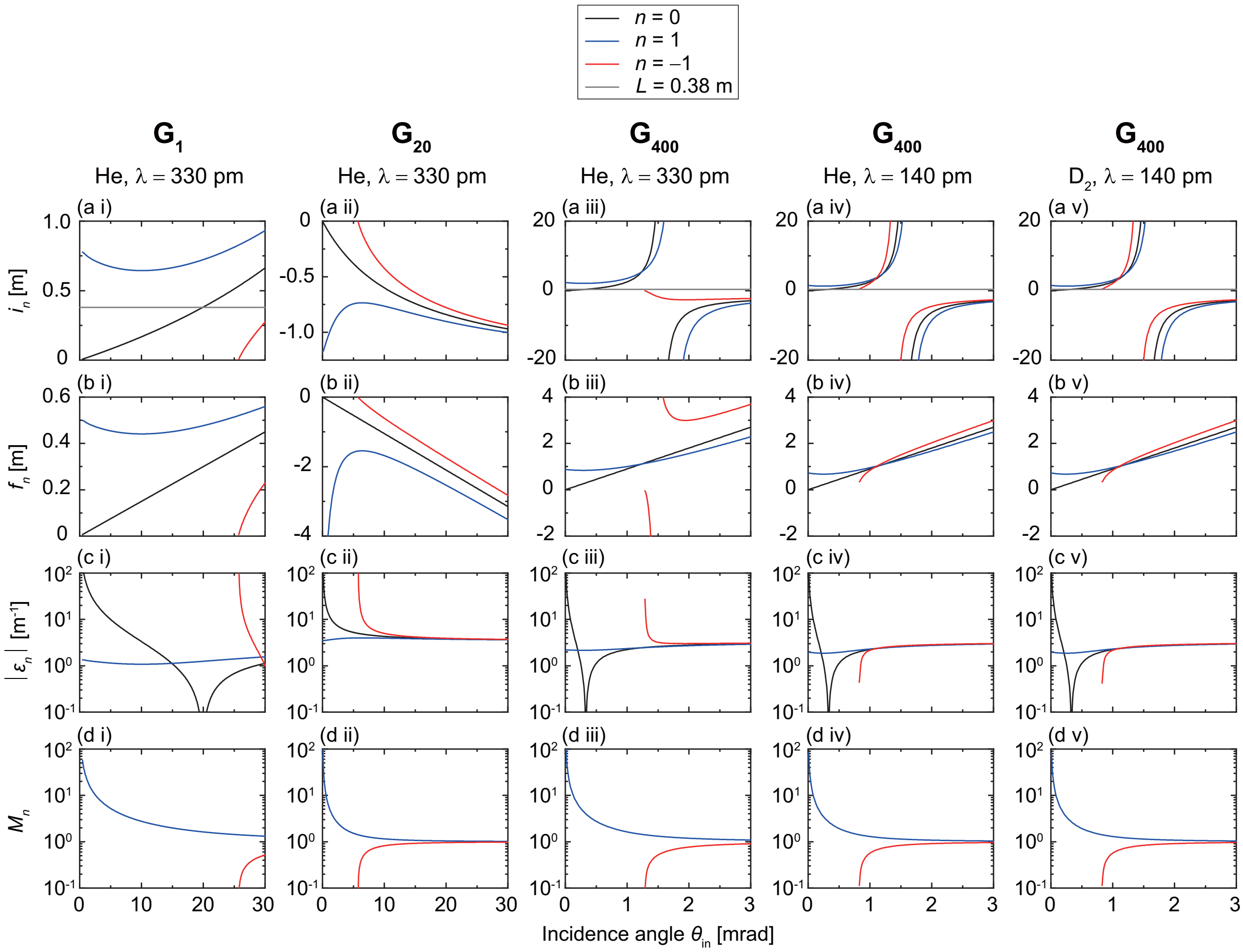

FIG. 6. (a) Image distance i_n, (b) focal length f_n, (c) focusing error ϵ_n, and (d) grating magnification M_n of the nth-order diffraction beam. The five columns correspond to the experimental conditions as in Fig. 5, respectively. Here G_1, G_{20}, and G_{400} are assumed to be cylindrical mirrors with curvature radii of $R = 30$, -210, and 1800 m, respectively. These graphs are plotted as functions of the incidence angle θ_{in}. The horizontal dotted line in (a) indicates the grating-detector distance $L = 0.38$ m.

contribution becomes pronounced only for an emerging peak close to the Rayleigh condition.

The width $W_n^{(4)}$ accounts for diffraction peak broadening resulting from angular dispersion due to the beam's finite velocity spread Δv. This effect is absent in the specular peak.

Finally, the finite size of the detector entrance slit S3 also contributes to the observed diffraction peak widths by the term $W^{(5)}$ of Eq. (5). This contribution is a constant 15 μm for all experimental conditions.

V. DISCUSSION

To assess the relative contributions of these five terms to W_n, we compare the measured W_n (symbols) with the corresponding calculated values for W_n, $W_n^{(1)}$, $W_n^{(2)}$, $W_n^{(3)}$, $W_n^{(4)}$, and $W^{(5)}$ (lines) in Fig. 5. The theoretical curves are determined considering the grating's macroscopic curvature radius R as the sole adjustable parameter. The angular widths w_n presented in Figs. 4(a)–4(e) are converted to linear widths W_n and presented in the five columns of Fig. 5, respectively.

For G_{20} the second data set measured at small incidence angles $\theta_{in} < 5.5$ mrad with tight beam collimation ($W_{S1} = 10$ μm and $W_{S2} = 15$ μm) [pale colored symbols in Fig. 4(b)] is characterized by a reduced angular width of $w_{in} = 0.081$ mrad. This corresponds to linear widths $W_{in} = 30.8$ μm and $W_G = 21.2$ μm. Figures 5(d)–5(f) include the corresponding calculations.

The breakdown of W_n into its five constituent terms in Fig. 5 highlights the dominant factors in each case. For G_1, for instance, the observed steep decays of W_n with incidence angle can be attributed to different factors for $n = 0$, 1, and -1. As illustrated in the graphs in Figs. 5(a)–5(c), at $\theta_{in} < 10$, 5, and 30 mrad, $W_0^{(1)}$, $W_1^{(1)}$ (red dashed curves), and $W_{-1}^{(4)}$ (blue dotted curve) predominantly influence the respective W_n values. Notably, the grating magnification is unity for the specular beam, which makes ϵ_0 the key determinant for $W_0^{(1)}$. Conversely, ϵ_1 varies by less than 33% in the given range of incidence angles, while the grating magnification term M_1 decreases tenfold [see Figs. 6(c i) and 6(d i)]. Therefore, the principal contributors to the steep decline in W_n for $n = 0$, 1, and -1 are the macroscopic curvature, grating magnification, and angular dispersion, respectively.

Similar to G_1, the decreases in W_0 and W_1 for G_{20} are primarily determined by the macroscopic curvature and grating magnification, respectively [see Figs. 5(d), 5(e), 6(c ii), and 6(d ii)]. However, unlike G_1, the 20-fold larger period of G_{20} diminishes the effect of angular dispersion [see Eq. (4)]. As a result, the influence of curvature on the reduction of W_{-1} becomes dominant.

For G_{400} the primary factor is $W_n^{(1)}$ (red dashed line) in most cases. Exceptions occur for W_{-1} at the Rayleigh conditions of $\theta_{\rm in} = \theta_{{\rm R},-1}$. At these conditions, θ_{-1} approaches 0, leading to large values for $W_{-1}^{(2)}$, $W_{-1}^{(3)}$, and $W_{-1}^{(4)}$.

Even though G_{400} is nearly flat with $R = 1800$ m, given the extreme grazing incidence conditions, the curvature still affects the peak-width variations. As can be seen in Figs. 4(c)–4(e), all three peak widths w_1, w_0, and w_{-1} can be narrower than the incident-beam width $w_{\rm in}$ resulting from beam focusing due to the concave curvature of the grating (refer to the graphs for W_0 and W_1 for G_{400} in Fig. 5).

In addition, the width hierarchy $w_1 > w_0 > w_{-1}$ visible in Fig. 4(d) presents a clear example for peak widths being dominated by grating magnification; the closer a beam propagates to the surface, the smaller its width. This trend is less clear in Figs. 4(c) and 4(e) where w_{-1} is not consistently the smallest width at the given incidence angles. Specifically, for incidence angles slightly larger than the negative-first-order Raleigh angle $\theta_{{\rm R},-1}$, w_{-1} exceeds both w_0 and w_1.

As shown in Figs. 5(i), 5(l), and 5(o), the larger contributions of the terms $W_{-1}^{(2)}$, $W_{-1}^{(3)}$, and $W_{-1}^{(4)}$ compared with $W_{-1}^{(1)}$ lead to broadening of W_{-1}. The small θ_{-1} close to Rayleigh conditions boosts these three terms. Interestingly, as shown in these graphs, $W_{-1}^{(2)}$ and $W_{-1}^{(3)}$ were the dominant factors for the He atom beams with two different λ, whereas $W_{-1}^{(4)}$ was the crucial factor for the D_2 molecular beam. This behavior can be attributed to the 13-times-larger velocity spread Δv of the D_2 beam compared with that of the He beam at identical velocity v.

VI. CONCLUSION

Our combined experimental and theoretical investigations of diffraction peak widths in GITEAS revealed the primary factors that induce variations in peak widths. Notably, the primary factor governing the width of diffraction beams varies depending on diffraction order, incidence angle, and grating period. Our study revealed the effects of macroscopic curvature, emerging beams, and grating magnification, which usually do not play a role in other scattering techniques, such as TEAS. Thus, our findings address potential ambiguities in interpreting diffraction data such as those presented in Fig. 3.

The comprehensive peak-width analysis conducted in this study lays the groundwork for extending the applicability of GITEAS to investigate the unique characteristics of dispersive interactions between atoms and thin-layer surfaces such as graphene sheets or few-layer hexagonal boron nitride, known for their flexibility. While recent theoretical investigations [29] have delved into these interactions, limited experimental studies are available. Additionally, this analysis can guide the design of atom optical components. Although both w_1 at $\theta_{\rm in} = 3$ mrad and w_{-1} near $\theta_{{\rm R},-1}$ in Fig. 4(a) are sufficiently broad for monochromator applications, only the negative-first-order diffraction beam is suitable for this purpose. This is because wavelength-dependent angular dispersion and wavelength-independent grating magnification primarily influence w_{-1} and w_1, respectively. Furthermore, peak-width analysis will become critical in atom interferometry using GITEAS.

ACKNOWLEDGMENTS

This study was supported by the National Research Foundation of Korea (Grants No. NRF-2020R1A2C3003701, No. NRF-2022M3C1C8094518, and No. NRF-2022M3C1C 8097622).

L.Y.K. and D.W.K. contributed equally to this work.

APPENDIX

For a cylindrically concave mirror with a curvature radius R, the object distance o and image distance i_n of the nth-order beam satisfy the following equation under grazing incidence conditions:

$$\frac{\theta_{\rm in}^{+} - \alpha/2}{o - R\alpha} + \frac{\theta_n^{+} + \alpha/2}{i_n + R\alpha} = \frac{2}{R} + \frac{(\theta_{\rm in}^{-} - \theta_n^{-}) + (\theta_{\rm in}^{+} - \theta_n^{+})}{W_{\rm G}/\theta_{\rm in}}. \tag{A1}$$

Here $\theta_{\rm in}^{+}$ and $\theta_{\rm in}^{-}$ represent the outermost values of the incidence angles that result in θ_n^{+} and θ_n^{-}, respectively. The incident beam spreads over a distance of $W_{\rm G}/\sin\theta_{\rm in}$ on the surface. This chord subtends an angle of 2α with respect to the center point of the grating's curvature, making α approximately equal to $W_{\rm G}/2R\sin\theta_{\rm in}$. Consequently, i_n varies as a function of $\theta_{\rm in}$, as depicted in Fig. 6(a) for the five experimental conditions. When $i_n = L$, a diffraction beam is focused on the detection plane. Equation (6) transforms into the thin-lens equation $1/o + 1/i_0 = 1/f_0$ for a specular beam of $n = 0$ with $f_0 = R\sin\theta_{\rm in}/2 \simeq R\theta_{\rm in}/2$ under grazing incidence conditions. Generally, $1/o + 1/i_n = 1/f_n$, with which we obtain f_n using i_n [see Fig. 6(b)]. Then $\epsilon_n = 1/L - i_n$. Figure 6(c) shows $|\epsilon_n|$ for the five experimental conditions. To elucidate the contributions of the focusing error ϵ_n and the grating magnification M_n to $W_n^{(1)}$, we plot M_n in Fig. 6(d).

[1] P. Scherrer, Nachr. Ges. Wiss. Göttingen, Math.-Phys. Kl. **2**, 98 (1918).

[2] J. I. Langford and A. J. C. Wilson, J. Appl. Cryst. **11**, 102 (1978).

[3] D. Balzar, N. Audebrand, M. R. Daymond, A. Fitch, A. Hewat, J. I. Langford, A. Le Bail, D. Louër, O. Masson, C. N. McCowan *et al.*, J. Appl. Cryst. **37**, 911 (2004).

[4] U. Holzwarth and N. Gibson, Nat. Nanotechnol. **6**, 534 (2011).

[5] D. M. Smilgies, J. Appl. Cryst. **42**, 1030 (2009).

[6] A. Mahmood and J.-L. Wang, Sol. RRL **4**, 2000337 (2020).

[7] D. Farías and K. H. Rieder, Rep. Prog. Phys. **61**, 1575 (1998).

[8] B. Poelsema, R. L. Palmer, G. Mechtersheimer, and G. Comsa, Surf. Sci. **117**, 60 (1982).

[9] *Scattering of Thermal Energy Atoms from Disordered Surfaces*, edited by B. Poelsema and G. Comsa, Springer Tracts in Modern Physics (Springer, Berlin, 1989), Vol. 115.

[10] P. Kirkpatrick and A. V. Baez, J. Opt. Soc. Am. **38**, 766 (1948).

[11] H. Mimura, S. Handa, T. Kimura, H. Yumoto, D. Yamakawa, H. Yokoyama, S. Matsuyama, K. Inagaki, K. Yamamura, Y. Sano *et al.*, Nat. Phys. **6**, 122 (2010).

[12] H. Yumoto, H. Mimura, T. Koyama, S. Matsuyama, K. Tono, T. Togashi, Y. Inubushi, T. Sato, T. Tanaka, T. Kimura *et al.*, Nat. Photon. **7**, 43 (2013).

[13] H. C. Schewe, B. S. Zhao, G. Meijer, and W. Schöllkopf, New J. Phys. **11**, 113030 (2009).

[14] H. Schief, V. Marsico, K. Kuhnke, and K. Kern, Surf. Sci. **364**, L631 (1996).

[15] V. Druzhinina and M. DeKieviet, Phys. Rev. Lett. **91**, 193202 (2003).

[16] B. S. Zhao, S. A. Schulz, S. A. Meek, G. Meijer, and W. Schöllkopf, Phys. Rev. A **78**, 010902(R) (2008).

[17] B. S. Zhao, H. C. Schewe, G. Meijer, and W. Schöllkopf, Phys. Rev. Lett. **105**, 133203 (2010).

[18] J. Fiedler, K. Lefmann, W. von Klitzing, and B. Holst, Phys. Rev. A **108**, 023306 (2023).

[19] J. H. Lee, L. Y. Kim, Y.-T. Kim, C. Y. Lee, W. Schöllkopf, and B. S. Zhao, Phys. Rev. Lett. **122**, 040401 (2019).

[20] *Modern Developments in X-Ray and Neutron Optics*, edited by A. Erko, M. Idir, T. Krist, and A. G. Michette, Springer Series in Optical Sciences (Springer, Berlin, 2008), Vol. 137.

[21] J. Als-Nielsen and D. McMorrow, *Elements of Modern X-Ray Physics*, 2nd ed. (Wiley, West Sussex, 2011).

[22] I. Estermann and O. Stern, Z. Phys. **61**, 95 (1930).

[23] R. E. Grisenti, W. Schöllkopf, J. P. Toennies, J. R. Manson, T. A. Savas, and H. I. Smith, Phys. Rev. A **61**, 033608 (2000).

[24] B. Poelsema, G. Mechtersheimer, and G. Comsa, Surf. Sci. **111**, 519 (1981).

[25] B. S. Zhao, G. Meijer, and W. Schöllkopf, Phys. Rev. Lett. **104**, 240404 (2010).

[26] B. S. Zhao, G. Meijer, and W. Schöllkopf, New J. Phys. **13**, 065017 (2011).

[27] B. E. Saleh and M. C. Teich, *Fundamentals of Photonics* (Wiley, New York, 2019).

[28] C. Palmer, *Diffraction Grating Handbook*, 8th ed. (MKS Instruments, New York, 2020).

[29] L. M. Woods, D. A. R. Dalvit, A. Tkatchenko, P. Rodriguez-Lopez, A. W. Rodriguez, and R. Podgornik, Rev. Mod. Phys. **88**, 045003 (2016).